AGU ADVANCING EARTH AND SPACE SCIENCE

JGR Atmospheres

RESEARCH ARTICLE
10.1029/2021JD035518

Key Points:

- Large moat size in long-lived concentric eyewall storms is explained with the scaling law of boundary-layer inner-eyewall pumping
- A large dimensionless moat implies a stronger boundary layer inflow due to a stronger pressure gradient force and a large moat distance
- Observations show decreases of vortex intensity, dimensionless moat, and inner-eyewall pumping in the replacement cycle on a phase diagram

Correspondence to:
S.-H. Su,
ssh3@g.pccu.edu.tw

Citation:
Kuo, H.-C., Tsujino, S., Hsu, T.-Y., Peng, M. S., & Su, S.-H. (2022). Scaling law for boundary layer inner eyewall pumping in concentric eyewalls. *Journal of Geophysical Research: Atmospheres*, *127*, e2021JD035518. https://doi.org/10.1029/2021JD035518

Received 5 JUL 2021
Accepted 18 JAN 2022

Scaling Law for Boundary Layer Inner Eyewall Pumping in Concentric Eyewalls

Hung-Chi Kuo[1], Satoki Tsujino[2], Tien-Yiao Hsu[3], Melinda S. Peng[4], and Shih-Hao Su[5]

[1]Department of Atmospheric Sciences, National Taiwan University, Taipei, Taiwan, [2]Meteorological Research Institute, Tsukuba, Japan, [3]Department of Earth System Science, University of California at Irvine, Irvine, CA, USA, [4]University of Colorado - Colorado Spring, Colorado Spring, CO, USA, [5]Department of Atmospheric Sciences, Chinese Culture University, Taipei, Taiwan

Abstract This study explains why observed storms with long concentric eyewall (CE) duration often have a large moat size. A series of slab boundary layer model experiments are conducted with the free atmosphere forcing from different CE structures. The experimental results indicate that the inner eyewall pumping (IEP), the maximum vertical motion at the inner eyewall region, increases with the increase in moat size d and vortex maximum wind v_m, the decrease in the inner eyewall radius r_m, and increase in inner eyewall vorticity. A scaling law is derived from hundreds of SBL experiments with four variables: IEP w_{in}, vortex inner radius r_m, vortex maximum wind v_m, and moat size d. The dimensionless scaling law is $w^* \sim \sqrt{d^*}$, where $w^* = w_{\mathrm{in}}/v_{\mathrm{m}}$, $d^* = \zeta d/c$, ζ is the vorticity $2v_m/r_m$, and c is a constant gravity wave speed. The moat size divided by the Rossby length c/ζ, the dimensionless moat size d^*, combines the effect of the moat size and the vortex pressure gradient force to accelerate the inflow and to enlarge the IEP for inner eyewall convection maintenance. A phase diagram of IEP with vortex structure dimensionless moat $\zeta d/c$ and vortex intensity v_m is constructed based on the scaling law for the aircraft and satellite observations. The eyewall replacement cycle may be viewed as the process to reduce the IEP from the decrease of the vortex intensity and the vortex size of the dimensionless moat. This leads to the ultimate disappearance of the inner eyewall.

Plain Language Summary The paper explains the large moat size in the long-lived concentric eyewalls tropical cyclones with boundary layer inner eyewall pumping (IEP) w_{in}. A scaling law from hundreds of experiments is found $w_{in} \sim v_m\sqrt{\zeta d/c} \sim v_m^{1.5} d^{0.5} r_m^{-0.5}$, where v_m is the vortex intensity, r_m the inner eyewall radius, d the moat size, ζ the vorticity $2v_m/r_m$ and c is a constant gravity wave speed. The radial inflow is greatly reduced when it passed through the outer eyewall region. The inflow then reaccelerates by the pressure gradient force (PGF). A decrease of Rossby length implies a larger PGF. The dimensionless moat $\zeta d/c$, the moat d divided by the Rossby length c/ζ, combines the effect of the moat size that allows the inflow to be accelerated and the effect of the inflow acceleration enhanced by the PGF. Large dimensionless moat is with a large IEP for the maintenance of the inner eyewall convection. A phase diagram of IEP with $\zeta d/c$ (structure) and v_m (intensity) variables is constructed to for aircraft and satellite data diagnosis. The demise of the inner eyewall may be viewed as the reduction of IEP by the decrease of storm intensity and the dimensionless moat size.

1. Introduction

Concentric eyewalls (CE), with a new eyewall formed outside the existing eyewall, and subsequent eyewall replacement cycle (ERC) in mature tropical cyclones (TCs) are important because of their impacts on intensity changes (Black & Willoughby, 1992; Houze et al., 2007; Kuo et al., 2009; Sitkowski et al., 2011; Willoughby et al., 1982; Wood et al., 2013). In general, CE duration is defined as the period from the formation of an outer eyewall to the complete decay of an inner eyewall in ERC. Based on aircraft observations, Black and Willoughby (1992) and Willoughby et al. (1982) suggested that TCs with an ERC process will experience a temporary weakening of the storm intensity. On the other hand, ERC may lead to increases in both storm size and integrated kinetic energy (Sitkowski et al., 2011). The duration time for CEs varies greatly. Radar observations of Typhoon Lekima in 2001 (Kuo et al., 2004) and the aircraft observation of Hurricane Andrew in 1992 (Willoughby & Black, 1996) both indicated that the ERC duration is approximately 6 hr. Sitkowski et al. (2011) found that the average ERC event as identified by aircraft data lasts for about 36 hr, which is much longer than the estimate from microwave satellite

data of 17.5 hr based on a study of 24 ERC events. The disagreement may be attributed to the fact that the satellite data are plane-view structures and the aircraft data are often one-direction profiles.

Yang et al. (2021) investigated the duration of TC CEs in different basins from microwave satellite imagery during 1997–2014. Their duration and structural parameters, including inner eyewall size, moat width, and outer eyewall width, were calculated. A long-lived CE (i.e., CEs with durations longer than 20 hr and with similar inner core size in the sequence of imagery) tends to have a larger size, mainly contributed by a larger moat (i.e., an annular region separating the two eyewalls) and a larger outer eyewall width. The inner eyewall size shows no significant difference between short-lived and long-lived CEs in the western North Pacific (WNP) but increases slightly and steadily with increasing CE durations in the Atlantic (ATL). Furthermore, the WNP has far more long-lived CEs than in ATL and in the eastern Pacific (EPAC). There are 83 (37) CEs with 19 (5) identified at WNP (ATL). The long-lived CEs in the WNP (Atlantics) is 23% (5%). The long-lived CE storms in the WNP is with an average ERC time of 31 hr, thus is important for intensity forecast. Their study strongly motivates to clarify the scientific reasons for the statistical relationship between the size parameters of the inner-core vortex (i.e., the inner eyewall size and moat and outer eyewall widths) and CE duration.

A case of multiple formations of CE storm is reported on western North Pacific Typhoon Soulik (2013; Yang et al., 2014). Typhoon Soulik (2013) had two anomalously long-lived CE episodes. The first (second) period was 25 hr (34 hr) long and occurred while Soulik was at category 4 (2) intensity. A large moat size and outer eyewall width were present in both CE periods. In contrast to microwave satellites and aircraft with relatively low observation frequency, ground-mounted radars have higher observation frequency and capture fine CE structures. Radar observations of the long-lived CE for TCs are rare because CEs often formed over open oceans. Figure 1 provides radar images for Typhoon Lekima (2019). The storm has its track near the east coast of Taiwan on 8–9 August 2019. The CE structure was captured by both radar networks in the Japanese Meteorology Agency (JMA) and the Central Weather Bureau (CWB) in Taiwan from 0400 UTC 08 to 1200 UTC 09 August 2019. Typhoon Lekima's CE structure was maintained for more than 30 hr with a traveling distance of about 600 km (Figure 1). Figure 1 indicates that the storm had a moat of approximately 40 km, an inner eyewall radius of 10 km, and strong inner eyewall deep convections throughout the period. Eventually, the inner eyewall dissipated when it made landfall in China. The above two cases demonstrated a good example that long-duration CE storms may have a large moat and strong inner eyewall convection.

There are implications of large moat size and wide outer width that may be relevant to the long-lived CEs. It is possible that larger CE storms simply end up taking a much longer time to contract and ERC. Moreover, the occurrence of barotropic instability (e.g., Kossin et al., 2000) will invalidate the axisymmetric state of the CE storms. Kossin et al. (2000) identified two types of barotropic instabilities in the vorticity field with CE structure; the instabilities across the outer eyewall and across the moat due to the sign reversal of the radial vorticity gradient (i.e., the Rayleigh necessary condition). These instabilities may work against the maintenance of the CE structure and the convections at the eyewalls. The large moat size and wide outer eyewall size may reduce the growth rate of instabilities and favor the maintenance of CE structure and convections.

Observational studies (Barnes & Powell, 1995; Barnes et al., 1983; Samsury & Zipser, 1995) indicated that the weakening of the inner eyewall is due to the blockage of water vapor transport by the outer eyewall. Satellite observations, however, indicate that the outer eyewall often is not in a complete axisymmetry fashion that may not totally block the moisture from the outside of the outer eyewall. From a modeling study, Tsujino et al. (2017) showed that the partial blockage of the water vapor supply may prolong the CE duration. In any event, the large moat size can be argued to favor the benign moisture pick up from the sea in the moat region to the inner eyewall region.

Another dissipation mechanism suggested that the development of an outer eyewall contributes to the inner eyewall demise by interrupting its low-level inflow (Houze et al., 2007; Samsury & Zipser, 1995) and the stabilization of inner eyewall convection (Rozoff et al., 2008). Yang et al. (2021) suggest that larger outer eyewall width often contains more cloud liquid water and maybe with more massive latent heat release. The geostrophic adjustment dynamics suggest that convection embedded in a wider outer eyewall (wide inertial stable region) favors the mass response from the convective heating and generates more kinetic energy in the form of gradient wind balance. The dynamically active outer eyewall, however, may have a detrimental impact on the inner eyewalls. Rozoff et al. (2008), who utilized Eliassen's transverse circulation equation to diagnose the secondary circulation,

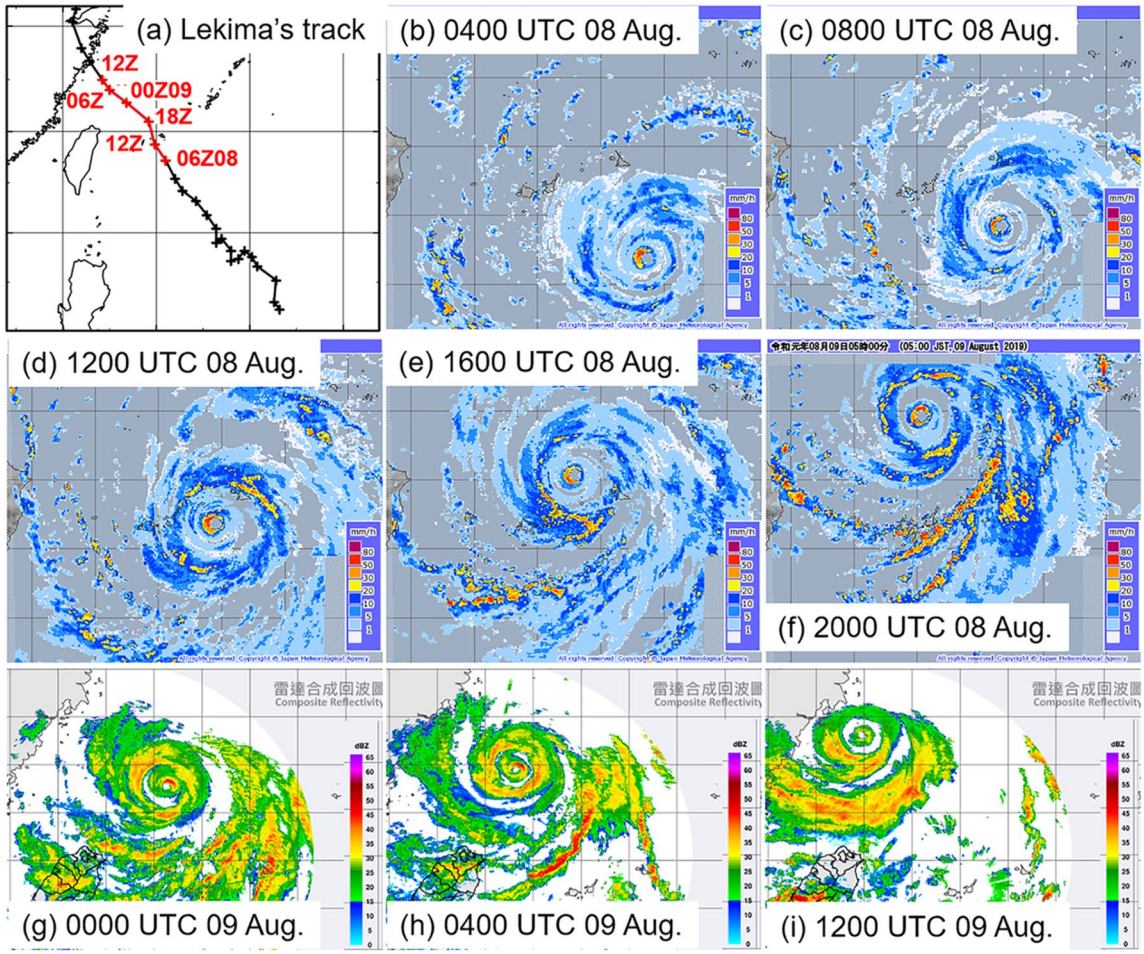

Figure 1. (a) Track and (b–i) radar images of Typhoon Lekima (2019) from (b–f) Japanese Meteorology Agency website (https://www.jma.go.jp/jma/indexe.html) and (g–i) Central Weather Bureau website (https://www.cwb.gov.tw/V8/E/W/OBS_Radar.html). The concentric eyewall structure last about 30 hr in the radar image. The track history was provided by the Regional and Mesoscale Meteorology Branch (http://rammb.cira.colostate.edu/products/tc_realtime/storm.asp?storm_identifier=WP102019), based on the National Hurricane Center, the Central Pacific Hurricane Center, and the Joint Typhoon Warning Center. Note that it is not any best tracks. The red color in the track history with 5° longitude and latitude grid lines shows period in which the CE structure was observed by the radars. The radar images with 1° longitude and latitude grid lines show a large moat width with strong inner eyewall convection in the period.

suggested that the free atmosphere subsidence warming in the moat region is enhanced by strengthening the outer eyewall convection with a wide inertial stability region. The subsidence warming could weaken the inner eyewall. A large moat size can presumably decrease the subsidence warming from convections in the outer eyewall. Zhou and Wang (2011) found that when the two eyewalls are close, there is a strong cold equivalent potential temperature advection to the inner eyewall within the boundary layer. As a result, the inner eyewall abruptly dissipates because the high moist entropy column can no longer be maintained. The wide moat size in the long-lived CE storms can reduce this negative impact of the dynamically active outer eyewall. Of interest, these results seem to link the width of the moat to the degree to which the outer eyewall impacts (negatively) the inner eyewall.

Questions are raised as what may control the size of large CE TCs? While the tangential wind profile of TCs may be idealized with a Rankine vortex structure, there are often skirt vorticity outside of the radius of maximum wind (Mallen et al., 2005). Kuo et al. (2008) proposed that a skirt TC with sufficient strength favors the formation of CE storms with a large moat. With the simulation of Hurricane Wilma (2005) using the WRF model, Lai et al. (2019) found that the type-2 barotropic instability dilutes the vorticity within the inner eyewall and the eye and that the unstable growth rate decreases as moat width increases. By quantitatively estimating inner-core tangential winds with high-frequent geostationary satellite images, Tsujino et al. (2021) indicated that a decrease in the tangential wind of the inner eyewall can be reasonably explained by radial transport of vorticity associated with asymmetric eddies during an ERC period of Typhoon Trami (2018). Yang et al. (2015) investigated the CE storms in WNP

under the environmental condition of El Nino-Southern Oscillation (ENSO). They found that the size of long-lived CE storms is larger in warm and normal episodes of the ENSO than that in cold episodes of the ENSO. The multiple CE formation cases that occurred in the warm and neutral episode may also lead to the formation of large size CE storms. These results suggest that the CE internal dynamical process, the TC track during the CE period and the environmental conditions are all critical to the CE size and duration.

Boundary layer (BL) dynamics are known to be important on TC intensification (Smith & Montgomery, 2016, Smith et al., 2009) and on the rotation convection paradigm (Montgomery & Smith, 2017). There are many studies on the dynamics within the BL including Abarca and Montgomery (2013), Huang et al. (2012), Kepert and Nolan (2014), Montgomery et al. (2014), and Slocum (2018). Shapiro (1983) used a slab BL (SBL) model of constant depth to study the wavenumber-one asymmetric convection under a translating hurricane. The modeling results were in general agreement with the observational study of Powell (1982). Williams et al. (2013) used an axisymmetric SBL model to interpret aircraft observations from Hurricane Hugo (1989). The aircraft observations indicate that the BL inflow decreases from approximately 22 m s^{-1} to zero over a radial distance of a few kilometers in Category 3 hurricanes, and the radial convergence can lead to updrafts exceeding 22 m s^{-1} at a height of 1000 m. They use the SBL model to demonstrate the importance of radial momentum nonlinear advection in producing shock-like structures such as that observed from the aircraft. The shock-like structure in the BL also leads to the development of large vorticity in a thin radial region in BL.

Kuo et al. (1999) studied with a non-divergent barotropic model explaining the cyclonically rotating elliptical eyewalls with vortex Rossby waves dynamics. Kuo et al. (2016) studied the WN2 deep convection located at the edge of the major axis in TCs with cyclonically rotating elliptical eyewalls. They employed a simple framework of a non-divergent barotropic model coupled with an asymmetric SBL model. In general agreement with the observations, the main results featured strong SBL model updrafts of the WN2 at the top of the BL from the local shock-like BL radial wind structure. Kuo et al. (2019) presented a cloud-resolving model that simulated the BL shock-like structure in the rapid intensification of Supertyphoon Haiyan (2013). Tsujino and Kuo (2020), with a 500 m high-resolution cloud-resolving model simulation, suggest that the coupling BL strong updraft and the large vorticity at the region of shock-like structure may result in convective potential vorticity (PV) tower of 200 PVU (PVU = 1×10^{-16} K m^2 kg^{-1} s^{-1}). Such hundreds of PVU convective PV tower has been reported from an observational study of Hurricane Patricia (2015) during its rapid intensification period (Martinez et al., 2019).

On the other hand, Kepert (2010a, 2010b) and Williams (2017) both indicated that SBL models produce excessively strong radial inflow, which implies excessively strong vertical velocities. Using BL models with different complexities, Kepert (2013) elucidated that the BL contributes to the formation of outer eyewalls through positive feedback among the local enhancement of the radial vorticity gradient, the frictional updraft, and convection. The friction-induced secondary circulation associated with the inner eyewall weakens as the outer wind maximum strengthens and/or contracts during an eyewall replacement cycle. Williams (2015) presented the difference between an SBL and multi-layer boundary layer simulations in that the inner core boundary layer flow in the slab model is dominated by the effects of horizontal advection and horizontal diffusion, leading to the development of shock structures in the model. Conversely, the inner core boundary layer flow in the multilevel model is primarily influenced by the effects of vertical advection and vertical diffusion, which eliminates shock structures in this model. Recently, Smith and Montgomery (2020) revisited the linear BL approximation expressing an Ekman balance and nonlinear BL in TCs. They documented that the inward nonlinear acceleration terms become comparable to the linear Coriolis acceleration terms in relatively narrow (i.e., inertially stable) vortices. It suggests that the BL in TCs is important for the evolution of the inflow in the BL and updraft on the top of the BL (and maintenance of the inner eyewall in cases of CE).

While the SBL models may be argued to produce excessively strong radial inflow and upward motion (Kepert, 2010a, 2010b; Williams, 2017), the SBL is a framework with a low degree of freedom. The SBL model catches dynamics of the nonlinear advective inward acceleration term in a relative narrow region (as is in Williams (2015) and Smith & Montgomery (2020)) and carries its simplicity for numerous experiments to understand the basic concept of flows within the BL. Moreover, the low degree of freedom in the framework allows us to find a scaling law for the IEP in the CE storms. A scaling law is a power law that asserts a proportional relationship between relevant quantities. In general, the finding of scaling law for a phenomenon in fluid systems can be largely helpful for understanding the phenomenon. In this study, we use the SBL model numerical experiments to explain the (positively) contribution of a large moat to the long-lived CE TCs. The results will be applied to

cases studied by Yang et al. (2013) and Yang et al. (2021). Section 2 describes the model and experiment design. The numerical results and the IEP scaling are in Section 3. Section 4 presents the IEP phase diagram with observations. The summary and concluding remarks are provided in Section 5.

2. Model Description and Experiment Designs

2.1. Slab-Boundary Layer Model

In this study, we use the SBL model for the calculation of the IEP in the CE vortex. The formulation of the SBL model in a polar coordinate centered at the storm is the same as in Schubert (2018) and Williams et al. (2013). The governing equations are

$$\frac{\partial u}{\partial t} = -u\frac{\partial u}{\partial r} - w^{-}\frac{u}{h} + \left(f + \frac{v + v_{gr}}{r}\right)(v - v_{gr}) - C_D U\frac{u}{h} + \kappa\frac{\partial}{\partial r}\left(\frac{\partial ru}{r\partial r}\right)$$

$$\frac{\partial v}{\partial t} = -\left(f + \frac{\partial rv}{r\partial r}\right)u - w^{-}\left(\frac{v - v_{gr}}{h}\right) - C_D U\frac{v}{h} + \kappa\frac{\partial}{\partial r}\left(\frac{\partial rv}{r\partial r}\right)$$

$$w = -h\frac{\partial ru}{r\partial r}$$

where u and v are radial and tangential wind of the BL, $w^{-} = (|w| - w)/2$ is the Ekman suction, v_{gr} is the gradient wind representing pressure gradient force from free-atmosphere above, $f = 5 \times 10^{-5}\ \mathrm{s}^{-1}$ is the Coriolis parameter, and the wind speed at 10 m height U follows the same 78% empirical value as in Williams et al. (2013):

$$U = 0.78\sqrt{u^2 + v^2}.$$

The drag coefficient C_D formula follows Powell et al. (2003):

$$C_D = 10^{-3}\begin{cases} 2.70/U + 0.142 + 0.0764U & \text{if } U \le 25\ \mathrm{ms}^{-1} \\ 2.16 + 0.5406\left[1 - \exp\left(-\frac{U - 25}{7.5}\right)\right] & \text{if } U \ge 25\ \mathrm{ms}^{-1}. \end{cases}$$

Numerical calculations are performed with the resolution of 100 m. We chose $\kappa = 1500\ \mathrm{m}^2\ \mathrm{s}^{-1}$ (Zhang & Montgomery, 2012), and $h = 1000$ m (Williams et al., 2013) in our calculations. In the overlying layer, the radial velocity is assumed to be negligible and the azimuthal velocity is assumed to be in gradient balance and to be a specified function of radius with a CE structure. The boundary layer flow is driven by the same radial pressure gradient force that occurs in the overlying fluid. The boundary condition at far field is the Neumann type of boundary condition with the r derivative of ru equals to zero and the boundary condition at the center of the storm is the Dirichlet type of boundary condition $u = 0$. We have compared our calculations with that of the asymmetric SBL model of Kuo et al. (2016) under the same symmetric CE structure. The results are identical in both models within machine accuracy.

2.2. Experimental Design

Our general experiment setting is a CE profile of the vorticity ζ in free-atmosphere

$$\zeta(r) = \begin{cases} \zeta_{\text{inner}} & \text{if} \quad r < r_m \\ 0 & \text{if} \quad r_m \le r < r_m + d \\ \zeta_{\text{outer}} & \text{if} \quad r_m + d \le r < r_m + d + w_{\text{out}} \\ 0 & \text{if} \quad r \ge r_m + d + w_{\text{out}} \end{cases}$$

where ζ_{inner} and ζ_{outer} are the vorticity strengths of inner and outer eyewalls, respectively. The parameters of r_m, d, and w_{out} are the radius of the inner eyewall, moat width, and outer eyewall width, respectively. The corresponding

Table 1
Parameters for the Experiments

Figure	Experiments	r_m (km)	v_m (m s^{-1})	d (km)	w_{out} (km)	ζ_{outer} (10^{-3} s^{-1})
Figure 2	A					4
	B	10	60	10	20	2
	C					1
Figure 3	A				30	
	B	10	60	10	20	2
	C				10	
Figure 4	A			10		
	B	10	60	20	20	2
	C			—	—	—
Figure 5	A		30			
	B	10	40	10	20	2
	C		60			
Figure 6	A	20				
	B	15	60	10	20	2
	C	10				

first maximum of tangential wind (vortex maximum wind) is at $r = r_m$ where $v_m = r_m\zeta_{inner}/2$. The pressure gradient force to drive the SBL model is determined from the radial profile of tangential wind v of the free atmosphere according to the ζ profile. In summary, the CE vortex in the free atmosphere is in gradient wind balance and the gradient wind is constant. The specified free atmospheric gradient wind and the associated balanced pressure field is to drive the BL inflow.

There are five vortex parameters for the experiments: ζ_{outer}, $w_{out,}$, d, v_m, and r_m. As will be shown in the next section, the thickness (w_{out}) and the vorticity strength (ζ_{outer}) of secondary eyewall do not affect the IEP. Thus, we employ sets of vortex parameters for the experiments r_m = 10, 20, 30, 40, 50 (km), v_m = 10, 20, 30, 40, 50, 60 (m s^{-1}), d = 10, 20, 30, 40, 50, 60, 70, 80, 90, 100 (km). The combination of these parameters gives a total of 300 numerical experiments. The IEP is calculated when the integration reaches a steady state. A steady state is often achieved with 2–3 hr model integration with the initial BL u (r, 0) = 0 and v (r, 0) = $v_{gr}(r)$. An example of the time evolution of SBL results to steady state can be found in Figure 6 of Williams et al. (2013). Note that we also performed experiments with κ = 1,500, 3,000, 4,500, 6,000 m^2 s^{-1}, and h = 1, 1.5, 2.0 km. There are a total of 3,600 experiments. The IEP $w_{in} \sim \sqrt{h/\kappa}$. For the concise in physical explanation, only the results with κ = 1,500 m^2 s^{-1} and h = 1000 m are shown in the paper.

3. Numerical Results

We perform experiments to describe the IEP dynamics with different CE vortex parameters. The experiments and parameters are listed in Table 1. Figure 2 illustrates the radial, tangential, and vertical wind profiles in the experiments of different outer eyewall vorticity but the same outer eyewall width as the forcing. The inner radius r_m, moat width d, and vortex maximum wind v_m are the same in the experiments. The upper three panels are the plane view of vorticity fields as the forcing to the SBL model. Dashed lines and solid lines are results from the free atmosphere and BL respectively. Note that the free atmosphere parameters (dashed lines) are given conditions constant with time and not model results. Figure 2 indicates that stronger outer eyewall vorticity in the free atmosphere can lead to a stronger BL pumping near the outer eyewall. With stronger vorticity, the secondary eyewall is being pushed more inward while the IEPs (the steady state maximum vertical velocity of the inner eyewall), however, are similar in magnitude and location.

Figure 3 is similar to Figure 2 except for the same outer eyewall vorticity but different outer eyewall width. The outer eyewall BL pumping is larger when the outer eyewall width is larger and the location centered at the width of the outer ring. With the same moat size and inner core, the IEP is of similar magnitude in these experiments. Figures 2 and 3 suggest that the IEP is not sensitive to the outer eyewall properties such as the outer eyewall width and vorticity. The outer eyewall region is zone of vorticity or inertial stable region. The radial inflow will be deflected when crossing the outer eyewall region. The radial flow speed will be reduced and the flow convergence lead to the outer eyewall BL upward motion. The radial inflow in these experiments is reduced to an approximate zero value when it passed through the secondary eyewall region. The inflow then begins to increase toward the inner eyewall under acceleration of the radial pressure gradient force. Thus, the IEP is not sensitive to the parameters of the outer eyewall. As discussed in Yang et al. (2021), the long-lived CEs maybe with a dynamically active outer eyewall with a wide width. Our results from Figures 2 and 3 will not be compromised by the presence of the wide dynamically active outer eyewall. The radial inflow speed certainly will be greatly reduced when it passed through an active secondary eyewall region. With the same r_m, v_m, and d, the IEP is similar. We will perform experiments with the same outer eyewall size and vorticity strength but with various parameters of r_m, v_m, and d.

Figure 4 is for the experiments of different moat widths (10 km in A and 20 km in B) and of single eyewall (C) in the free atmosphere forcing. The outer eyewall width and vorticity values are the same in experiments A and B as well as the inner eyewall radius and vorticity. Figure 4 indicates the existence of super-gradient (sub-gradient)

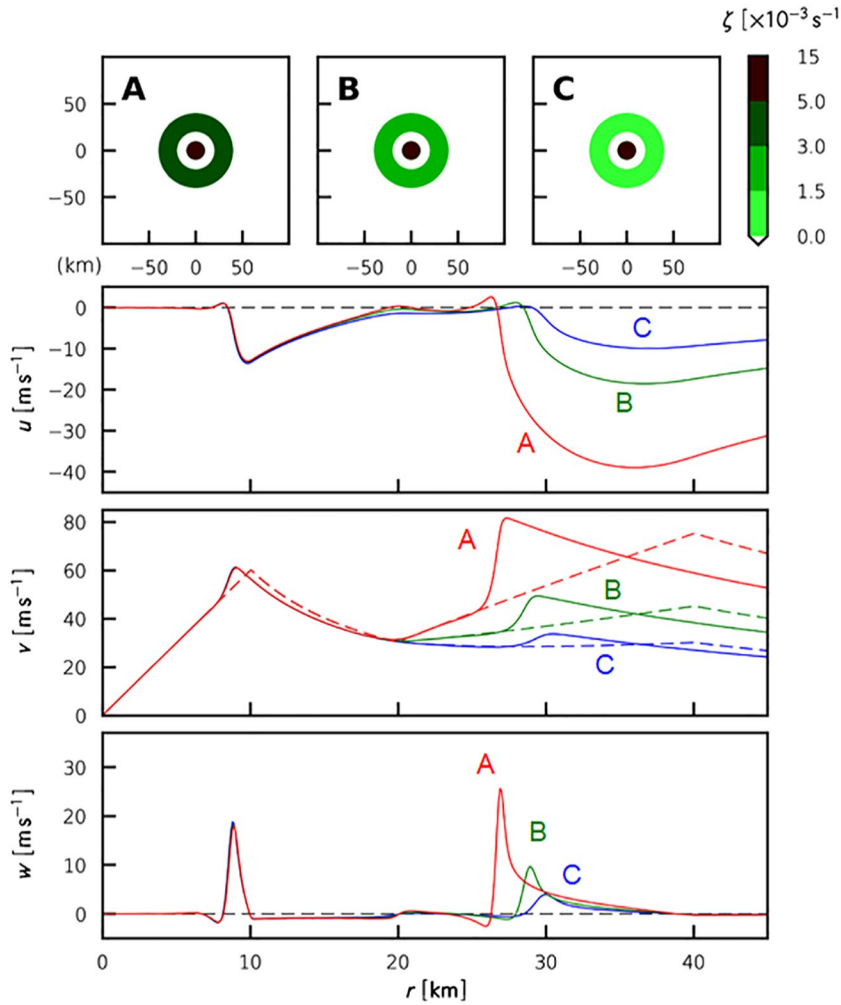

Figure 2. Experiments of different outer eyewall vorticity but the same outer eyewall width. The inner radius r_m, moat width d and v_m are the same in the experiments. Upper three panels are the plane view of vorticity fields. Lower three panels u, v, and w are radial, tangential and vertical wind profiles, respectively. Dashed lines and solid lines are from the free atmosphere and BL steady state results, respectively. Dash lines are given conditions constant with time, not model results.

winds inside (outside) the local radius of maximum wind (RMW) in the BL. In general, the super-gradient wind can be maintained by the near conservation of angular momentum associated with the large radial inflow. The BL inflow decreases from approximately 22 m s^{-1} (C), 18 m s^{-1} (B), and 13 m s^{-1} (A) to zero near the RMW over a radial distance of 6 km near the inner eyewall. The radial flow profile indicates a shock-like structure and IEP in the BL, similar to that of Williams et al. (2013). Figure 4 suggests that the strongest updraft is in the single eyewall experiment C. The A and B experiments are with weaker updraft because the presence of the outer eyewall reduces the inflow speed to zero at the inner edge of the outer eyewall, and thus is detrimental to the IEP. Meanwhile, the IEP is stronger in the B experiment as compared to that in the A experiment. It suggests that a larger moat size in the B experiment allows the inflow to be reaccelerated toward the inner eyewall in a long time than that of the A experiment.

Figure 5 considers a set of experiments with varying vortex maximum wind v_m but kept the moat width and inner eyewall radius constant. The outer eyewall width and outer eyewall vorticity are also kept constant. This set of experiments suggests that the IEP is proportional to v_m. Figure 6 is similar to Figure 5, except for the varying of inner eyewall radius but kept the moat width and vortex maximum wind constant. This set of experiments suggests that IEP increases with an increase of the inner eyewall vorticity or a decrease of inner eyewall radius. In summary, the experiments represented in Figures 4–6 suggests that IEP increases with an increase in moat size d, the vortex maximum wind v_m, a decrease in inner eyewall radius r_m, and an increase in the inner eyewall vorticity.

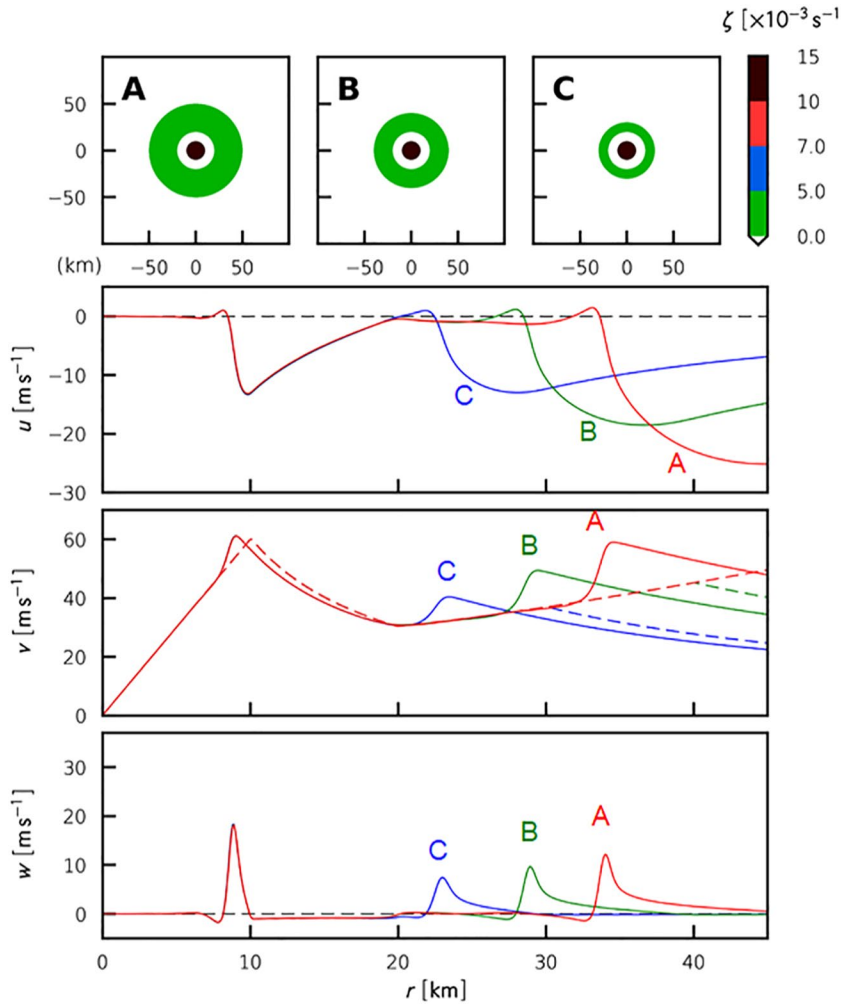

Figure 3. Similar to Figure 2 except for the experiments of different outer eyewall width but the same outer eyewall vorticity.

To explore the functional dependency of the IEP with the vortex parameters, we perform experiments with parameters r_m = 10, 20, 30, 40, 50 (km), v_m = 10, 20, 30, 40, 50, 60 (m s^{-1}), and d = 10, 20, 30, 40, 50, 60, 70, 80, 90, 100 (km). From the combined total of 300 experiments, we attempt to construct a relationship among the above three controlling parameters and the resulting IEP. Even the IEP increases with the increases of the moat size as suggested by Figure 4, however, there must be some limitations of the moat size to the increase of the IEP. Namely, the acceleration toward the storm center cannot speed up the inflow originated from a distance very far away from the center. Thus, we tested the dependency of the IEP with different constraints and have found that the constraint of $\sqrt{v_m/d} > 0.03$ (v_m and d both in SI unit) yields the optimal fitting with $R^2 = 0.93$. The regression line equation is $w_{in} = 0.017 * v_m^{1.5} r_m^{-0.5} d^{0.5} + 0.85$. The constraint of $\sqrt{v_m/d} > 0.03$, for example, selects the experiments with moat size smaller than 50 km (30 km) for the v_m of 50 m s^{-1} (30 m s^{-1}). The number of the sampling experiments with the constraint is about 100. As seen in Figure 7 the relationship is $w_{in} \sim v_m^{1.5} d^{0.5} r_m^{-0.5} \sim v_m \sqrt{\zeta d}$, where $\zeta = 2v_m/r_m$ is the inner vorticity strength. Note that without the imposed constraint of $\sqrt{v_m/d} > 0.03$, the scaling law is the same except that the R^2 is 0.89. Without the constraint, the IEP data has many horizontal spreads when the moat size is sufficiently large. The horizontal spread suggests that the IEP is saturated with the moat size. This leads to the scaling law with the constraint and a slightly better R^2 in our analysis.

The physics behind the scaling in Figure 7 can be explained by defining the dimensionless variables w^*, u^*, and d^*, where $w^* = w_{in}/v_m$, $u^* = u/v_m$, $d^* = \zeta\, d/c$. The dimensionless radial flow and IEP are defined with the scaling of the vortex maximum wind v_m. The dimensionless moat width d^* is the moat size d scaled by the vortex

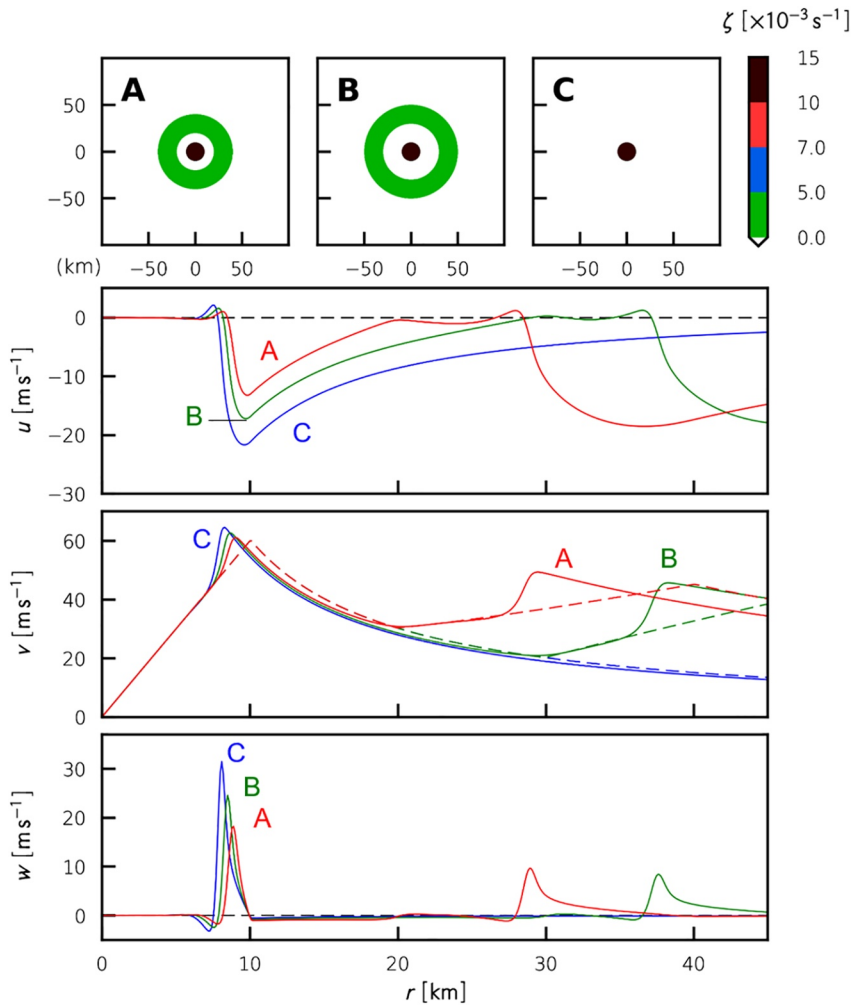

Figure 4. Similar to Figure 2 except for the experiments of different moat widths (20 km in A and 30 km in B and single eyewall C). The outer eyewall width and the vorticity value are the same in the experiments A and (b). The inner eyewall radius and vorticity are the same in the experiments.

Rossby radius of deformation c/ζ, where the c is the gravity wave speed of first internal vertical mode. This gravity wave speed is introduced for the physical interpretation with Rossby radius of deformation similar to that of Schubert (2018) in treating the dimensionless length in the TC environment. The gravity wave speed is a constant and is not affecting the proportionality of the dynamic parameters and the scaling law. The c of 50 m/s of the first internal mode is a dominant mode with the convective heating in the TC. The 50 m/s also makes the value of dimensionless moat approximately in the range of one to 10 for an easier discussion. The dependency of r_m variable in the scaling law is incorporated into the vorticity variable and the Rossby radius of deformation. Previous studies have indicated that TC intensification is often accompanied by a decrease of Rossby radius of deformation, which causes not only more mass response to the convective heating in pressure deficit but also a vertically elongated pressure deficit pattern near the center of the storm (e.g., Tsujino & Kuo, 2020). The vertical elongated pressure deficit pattern is with a larger horizontal pressure gradient. The large horizontal pressure gradient can enhance the BL radial inflow. Thus, we can view the dimensionless moat (i.e., the moat divided by the Rossby radius of deformation) combines the effects of the physical size of the moat and the vortex pressure gradient force to accelerate a near-zero speed of inflow from the inner edge of outer eyewall to the inner eyewall. The acceleration leads to a large IEP for the inner eyewall maintenance.

For the BL radial inflow in the moat under the inward acceleration from the core region under the constraint of $\sqrt{v_m/d} > 0.03$, we have $d^* \sim u^{*2}$ in that the work done of mean inward acceleration times the d^* is proportional to the dimensionless radial flow kinetic energy u^{*2}, and also the dimensionless IEP is proportional to

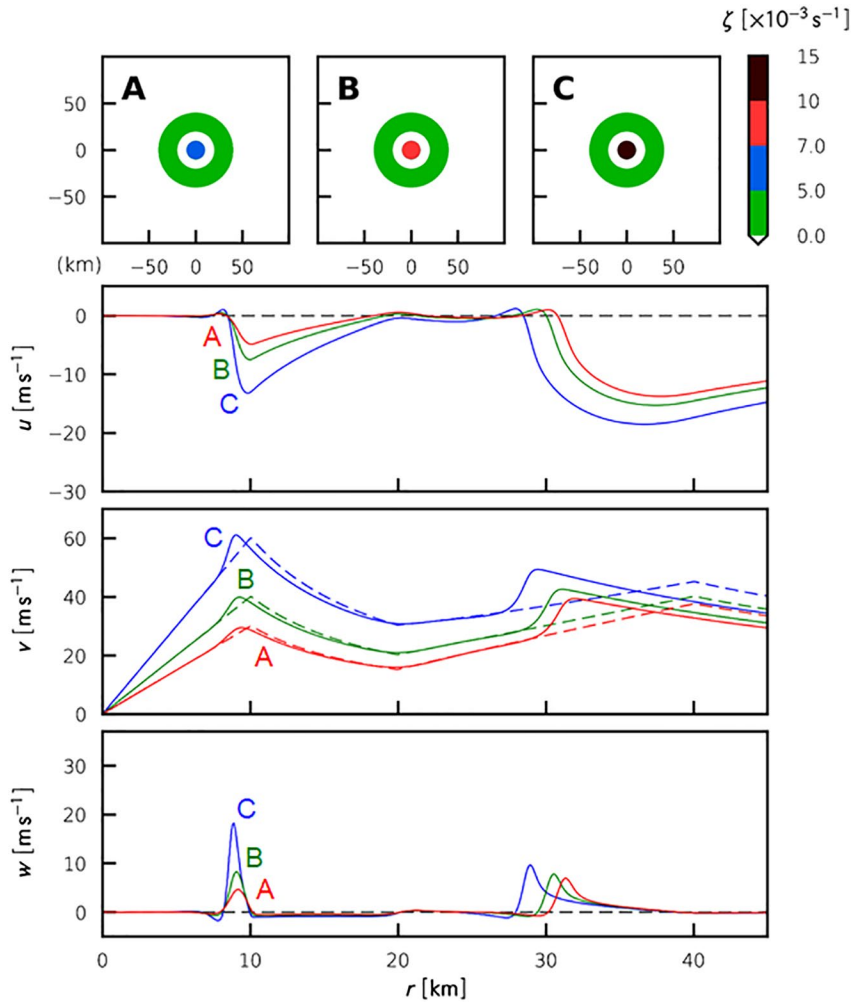

Figure 5. Similar to Figure 2 except for experiments with different vortex maximum wind. The inner eyewall radius, moat width, and outer eyewall width, and outer eyewall vorticity are the same in all experiments.

the dimensionless radial inflow such that $w^* \sim u^*$. Here the constraint of $\sqrt{v_m/d} > 0.03$ is placed for reasonably large vorticity greater than 4×10^{-4} s^{-1} for a mature TC. The above dependency in dimensionless time implies that $w^* \sim \sqrt{d^*}$, which is the relationship of our dimensionless variables. In dimensional form, it yields $w_{in} \sim v_m\sqrt{d^*} \sim v_m \sqrt{\zeta d/c} \sim v_m^{1.5} d^{0.5} r_m^{-0.5}$, which is consistent with our SBL experiments. The vortex intensity v_m and vortex structure dimensionless moat width d^* are important dynamic parameters for the IEP.

4. Phase Diagram of Inner Eyewall Pumping

The scaling law indicates that IEP is a function of the structure variable dimensionless moat and the intensity variable. With the scaling law of $w_{\text{in}} \sim v_m \sqrt{\zeta d/c}$, we constructed a phase diagram of IEP w_{in} in terms of vortex intensity v_m and vortex structure in dimensionless moat d^*, to aid the interpretation of CE observations. The essence of the diagram is the vortex intensity v_m (ordinate), the vortex size dimensionless moat size $d^* = \zeta d/c$ (abscissa), and contours of IEP computed from the scaling law. The dimensionless moat is used in the diagram, rather than the physical moat size, because it combines the effect of the physical size of the moat that allows the inflow to be accelerated and the effect of the inflow acceleration enhanced by the pressure gradient force. It is a more relevant dynamic structure parameter for ERC. We use gravity wave speed of $c = 50$ m s^{-1} of the first internal vertical mode in the vortex Rossby radius of deformation c/ζ (Schubert, 2018) to scale the moat size. With the CE vortex intensity v_m, and size parameters r_m, and d from the observation, an IEP can be calculated. Figure 8 is a construction of the IEP diagram with v_m and d^* for the aircraft observations. The time after

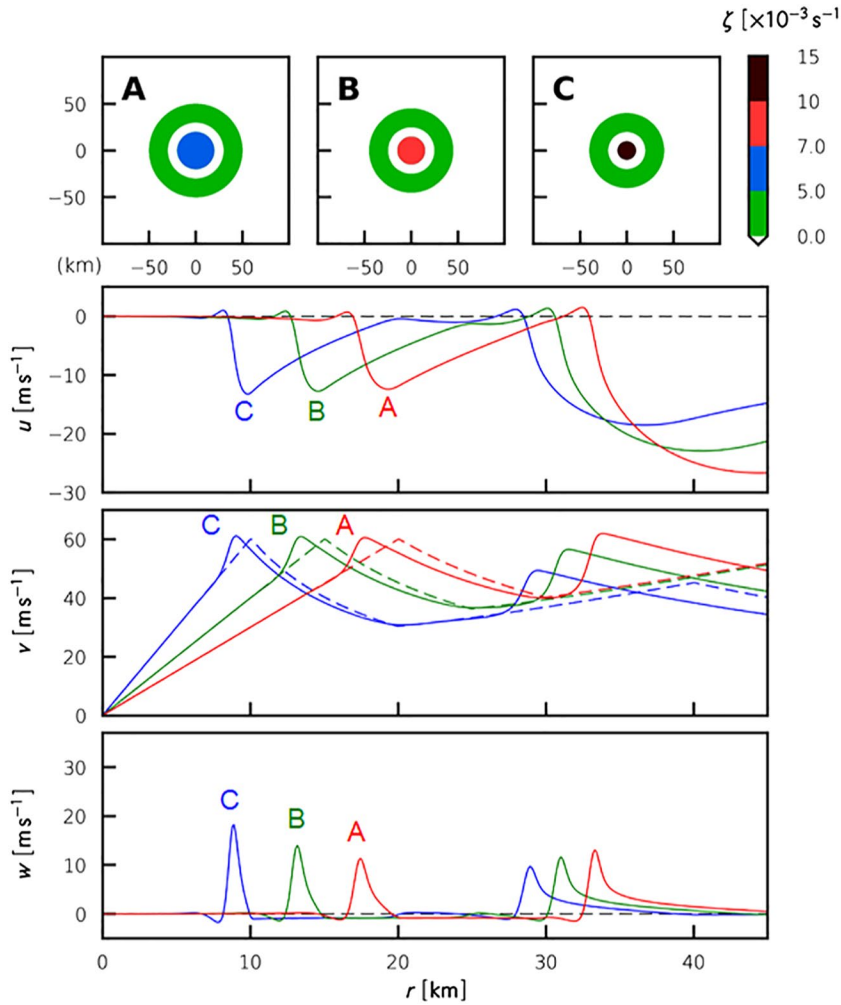

Figure 6. Similar to Figure 2 except for experiments with different inner eyewall radius. The moat width, vortex maximum wind, outer eyewall width and vorticity are the same in all experiments.

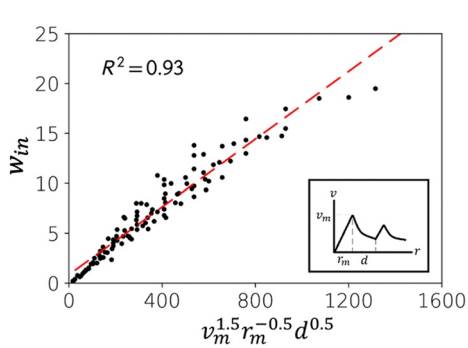

Figure 7. The scaling of inner eyewall pumping w_{in} in terms of the moat width d, inner core vorticity, and inner core radius in the slab boundary experiments. Experiment parameters are $r_m = 10, 20, 30, 40, 50$ (km), $v_m = 10, 20, 30, 40, 50, 60$ (m s^{-1}), $d = 10, 20, 30, 40, 50, 60, 70, 80, 90, 100$ (km). The plot uses the experiments with the condition $\sqrt{v_m/d} > 0.03$. The regression line equation is $w_{in} = 0.017 * v_m^{1.5} r_m^{-0.5} d^{0.5} + 0.85$. See the text for the discussion.

the CE formation in the storms is indicated in the diagram. The moat size after the CE formation is determined from the aircraft observation while it is possible to identify two peaks in the tangential wind. The aircraft data are based on the following papers: Hurricanes Diana (1984), Floyd (1999), and Ivan (2004) from Sitkowski et al. (2011), Hurricane Gilbert (1988) from Black and Willoughby (1992), Hurricane Frances (2004) from Rozoff et al. (2008), Hurricane Rita (2005) from Bell et al. (2012), and Typhoon Sinlaku (2008) from Sanabia et al. (2015).

According to the scaling law, the upper-right area (lower-left area) in Figure 8 is with stronger (weaker) IEP. The data points moved from an area of large vortex maximum wind v_m and dimensionless moat d^*, to an area of small v_m and d^* during the ERC process. Note that reducing the dimensionless moat may be due to the decrease of either vortex intensity v_m and/or the moat size. In fact, for CE storms, the changes of TC intensity and moat size can be asynchronous. For example, in Typhoon Sinlaku (2008) both the moat size and intensity were decreased from (66 km, 41 ms^{-1}) to (32 km, 23 ms^{-1}) during a 27 hr ERC process. On the other hand, Hurricane Gilbert (1988) moat size of 50 km and inner radius of 12.5 km stayed almost the same but the intensity

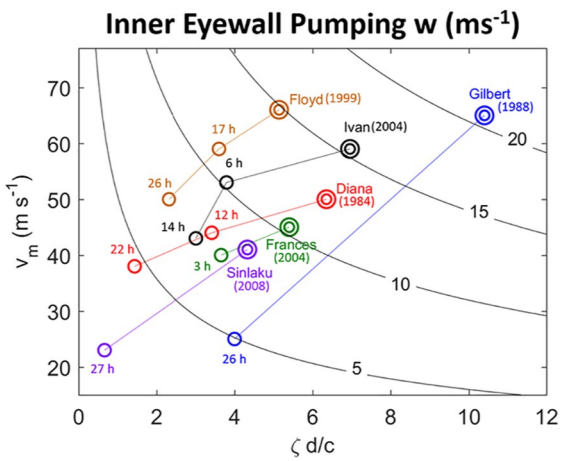

Figure 8. A phase diagram of inner eyewall pumping (IEP) w_{in} as a function of the vortex maximum wind v_m and the dimensionless moat $d^* = \zeta d/c$. Black contour denotes the IEP in the unit of (m s^{-1}) based on the scaling law. Each CE case based on aircraft observations is plotted on the diagram with markers of double circles and single circle. The double circles are storms at the CE formation and the single circles indicate storms in the eyewall replacement cycle (ERC) process. The time indicated in each single circle symbol shows the time after the CE formation in the ERC process.

decreased from 65 to 25 ms^{-1}. Figure 8 indicates the CE cases are with both decreasing dimensionless moat and IEP in the ERC process. In terms of the vortex intensity and structure parameters, the ERC process may be interpreted as the decrease of intensity v_m and dimensionless moat size d^*. Figure 8 suggests that the CE storms at the beginning of the ERC process, are with v_m greater than 40 m s^{-1} and d^*greater than 4 according to the aircraft observations. The ERC process reduces the d^* to values smaller than 4. These numbers can serve as a starting point for further examinations of ERC cases. Note that the Lekima (2019) case is with 65 m s^{-1} maximum wind from JTWC and moat size (inner eyewall radius) of 40 km (10 km) from the JMA radar image at 0600 UTC 08 August 2019. The d^* is approximately 10 at this time. In the end of the 30-hr CE duration, the maximum wind is approximately 50 m s^{-1}, the d^* is about 7. Lekima (2019) appears with large d^* in the 30 hr CE duration and is in general agreement with the analysis of Figure 8.

Figure 9 contains CEs from 1997 to 2014 in WNP based on the microwave satellite data as identified by the objective method of Yang et al. (2013). The moat size and the inner radius are determined from the microwave satellite data at the time when the CE storms are identified. The typhoon intensity is from JMA with 10 min averaged wind and from the Joint Typhoon Warning Center (JTWC) with 1 min averaged wind. The data is stratified with the CE duration of 20 hr for the long-lived and short-lived CE categories (Yang et al., 2013). Note that the No Replacement Cycle cases in Yang et al. (2013) are with the part of the outer eyewall diminished under strong vertical wind shear. It is under strong environmental control and is not included in the present analysis. Despite the difference of typhoon intensity in both agencies of JMA and JTWC, the v_m and d^* are in general larger in the long-lived CE cases as compared to that with the quick demise of inner eyewall in ERC cases. Rozoff et al. (2008) suggested the detrimental effect to the inner eyewall by the increase of free atmosphere subsidence warming and static stability by the contraction of the outer eyewall during ERC. Our results, from a BL perspective, suggest that the outer-eyewall contraction (i.e., reduction of the moat width and inner eyewall intensity)

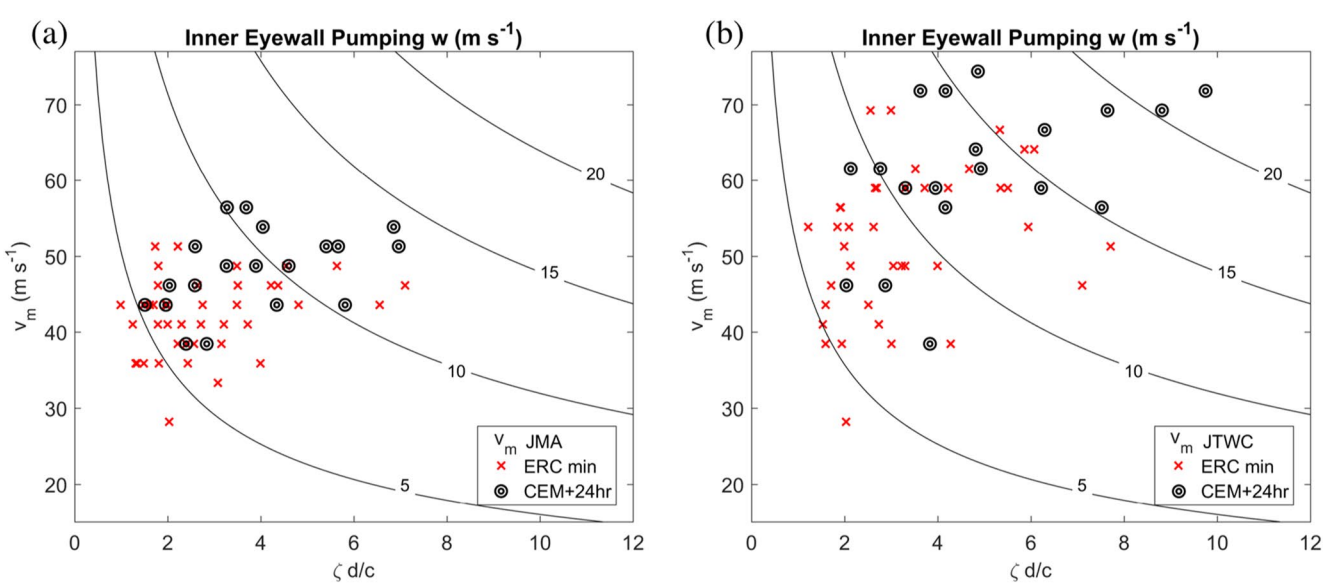

Figure 9. As in Figure 8, except for CE storms in western North Pacific from 1997 to 2014. The moat size and inner eyewall radius are estimated from microwave satellite images according to Yang et al. (2013). The storm intensity is based on (a) the JMA with 10 min averaged wind speed and (b) the Joint Typhoon Warning Center with 1 min averaged wind speed. Red crosses and black double circles denote short-lived and long-lived CE cases, respectively. In the short-lived CE cases, the minimum wind speed within 24 hr after the CE formation time is used as the storm intensity. In the long-lived CE cases, the wind speed at 24 hr after the CE formation is used as the storm intensity. CEM stands for "Concentric Eyewall Maintained"; the CEM cases are the CE structure is maintained for more than 20 hr and the inner cores in the sequence of imagery have a similar size.

can efficiently reduce the IEP and weaken the inner eyewall. Figures 8 and 9 highlight the importance of vortex maximum wind, inner eyewall vorticity, and large moat size in regulating strong IEP in the CE storms. The two relevant vortex parameters for ERC, from a BL IEP perspective, are the intensity v_m and the structure variable of dimensionless moat d^*.

5. Summary and Concluding Remarks

Yang et al. (2021) examines the long-lived CE structure in TCs in different basins and find that the long-lived CE tends to have a larger size, mainly contributed by a larger moat and a larger outer eyewall width. The WNP has far more long-lived CEs than in ATL and in EPAC. The long-lived CEs in the WNP (ATL) is 23% (5%). The long-lived CE storms in the WNP is with an average ERC time of 31 hr, thus is important for intensity forecast and research.

The focus of the paper is to provide BL perspective on why the long-lived CE TCs often with a large moat size. The main result is the IEP scaling law based on the SBL model experiments with vortex parameters $w_{in} \sim v_m\sqrt{\zeta d/c} \sim v_m^{1.5} d^{0.5} r_m^{-0.5}$, where ζ is the vorticity $2v_m/r_m$ and c is a constant gravity wave speed introduced for the physical reasoning and will not affect the scaling law proportionality. The outer eyewall region is a zone of vorticity or inertial stable region. The SBL model radial inflow is reduced to an approximate zero value when it passed through the outer eyewall region. The inflow then begins to increase toward the inner eyewall under acceleration of the radial pressure gradient force. The IEP is not sensitive to the parameters of the outer eyewall. The wide-width dynamically active outer eyewall in the long-lived CEs certainly support this argument. TC intensification is often accompanied by a decrease of Rossby radius of deformation, which causes not only more pressure deficit response to the convective heating, but also a more vertically elongated pressure deficit pattern near the center of the storm (e.g., Tsujino & Kuo, 2020). The vertical elongated pressure deficit pattern is with a larger horizontal pressure gradient. Both the large moat size and the large pressure gradient force can enhance the BL radial inflow to a large IEP for the maintenance of the inner eyewall. We highlight the importance of the dimensionless moat (i.e., the moat divided by the Rossby radius of deformation $\zeta d/c$) to combine the effects of the moat size and pressure gradient force to accelerate a near-zero speed of inflow from the inner edge of the outer eyewall toward the inner eyewall.

A phase diagram of IEP based on the scaling law is constructed to aid the interpretation of aircraft and satellite CE data. The IEP is a function of the vortex structure variable dimensionless moat d^* and intensity variable v_m of the storm. The IEP in the CE storms becomes weaker in the ERC process. It further suggests that strong IEP is with large d^* and v_m in the observations. Aircraft observations suggested that CE storms are with the v_m greater than 40 m s^{-1} and the d^* greater than 4. Typhoon Lekima (2019) is estimated to have a d^* of 7–10 in the 30-hr CE duration period. The vortex maximum wind v_m and the dimensionless moat d^* are the essential parameters in this IEP argument. The ERC may be viewed as the process reduce both the intensity v_m and the structure size dimensionless moat d^*. The decrease in the two vortex parameters of intensity and dynamic size eventually leads to the ultimate demise of the IEP and inner eyewall.

With the limitation of the SBL model, and in its neglect of vortex potential vorticity dynamics time evolution, secondary circulation, and diabatic heating, our argument falls well short of a complete theory. However, the SBL model for its simplicity but still possesses the complexity of nonlinear BL dynamics, allows an investigation of CE parameters for IEP with hundreds of experiments. It does not seem to be unreasonable to expect the essential role of the large dimensionless moat in radial inflow acceleration to the storm center and moisture pick up to sustain the inner eyewall convection. The scaling law and the constructed phase diagram aid our interpretation of the ERC observations with IEP, vortex intensity v_m, and vortex structure in dimensionless moat d^*. Careful analysis of fine-scale simulations of the BL in full physics models will be the future work.

Conflict of Interest

The authors declare no conflicts of interest relevant to this study.

Data Availability Statement

We would also like to show our gratitude to the Taiwan Central Weather Bureau, Japan Meteorological Agency, and the Navy Research Lab (NRL) for providing the observation data. Those data can be accessed via the NRL Tropical Cyclone Page (https://www.nrlmry.navy.mil/TC.html), the Japan Meteorological Agency website (https://www.jma.go.jp/jma/indexe.html), and the Taiwan Central Weather Bureau website (https://www.cwb.gov.tw/V8/E/W/OBS_Radar.html).

Acknowledgments
The authors would like to thank Dr. W. H. Schubert and P. Ciesielski for their valuable and constructive comments. We acknowledge Mr. Cheng-Yu Chen's help in preparing the figures and computation. We appreciate three anonymous reviewers as their comments helped us better revise our paper. This work was supported by MOST Taiwan (Ministry of Science and Technology in Taiwan) under grant MOST-109-2111-M-002-008, MOST-109-2625-M-002-021, MOST-108-2119-M-002-022, MOST-107-2628-M-002-016, MOST-106-2119-M-002-016, and the Office of Naval Research Global under grant N62909-15-1-2008.

References

Abarca, S. F., & Montgomery, M. T. (2013). Essential dynamics of secondary eyewall formation. *Journal of the Atmospheric Sciences*, *70*, 3216–3230. https://doi.org/10.1175/JAS-D-12-0318.1

Barnes, G. M., & Powell, M. D. (1995). Evolution of the inflow boundary layer of Hurricane Gilbert (1988). *Monthly Weather Review*, *123*, 2348–2368. https://doi.org/10.1175/1520-0493(1995)123<2348:EOTIBL>2.0.CO;2

Barnes, G. M., Zipser, E. J., Jorgensen, D., & Marks, F., Jr (1983). Mesoscale and convective structure of a hurricane rainband. *Journal of the Atmospheric Sciences*, *40*, 2125–2137. https://doi.org/10.1175/1520-0469(1983)040<2125:MACSOA>2.0.CO;2

Bell, M. M., Montgomery, M. T., & Lee, W. (2012). An axisymmetric view of concentric eyewall evolution in Hurricane Rita (2005). *Journal of the Atmospheric Sciences*, *69*, 2414–2432. https://doi.org/10.1175/JAS-D-11-0167.1

Black, M. L., & Willoughby, H. E. (1992). The concentric eyewall cycle of Hurricane Gilbert. *Monthly Weather Review*, *120*, 947–957. https://doi.org/10.1175/1520-0493(1992)120<0947:TCECOH>2.0.CO;2

Houze, R. A., Jr, Chen, S.-S., Smull, B. F., Lee, W.-C., & Bell, M. M. (2007). Hurricane intensity and eyewall replacement. *Science*, *315*, 1235–1239. https://doi.org/10.1126/science.1135650

Huang, Y., Montgomery, M. T., & Wu, C. (2012). Concentric eyewall formation in Typhoon Sinlaku (2008). Part II: Axisymmetric dynamical processes. *Journal of the Atmospheric Sciences*, *69*, 662–674. https://doi.org/10.1175/JAS-D-11-0114.1

Kepert, J. D. (2010a). Slab- and height-resolving models of the tropical cyclone boundary layer. Part I: Comparing the simulations. *Quarterly Journal of the Royal Meteorological Society*, *136*, 1689–1699. https://doi.org/10.1002/qj.667

Kepert, J. D. (2010b). Slab- and height-resolving models of the tropical cyclone boundary layer. Part II: Why the simulations differ. *Quarterly Journal of the Royal Meteorological Society*, *136*, 1700–1711. https://doi.org/10.1002/qj.685

Kepert, J. D. (2013). How does the boundary layer contribute to eyewall replacement cycles in axisymmetric tropical cyclones? *Journal of the Atmospheric Sciences*, *70*, 2808–2830. https://doi.org/10.1175/JAS-D-13-046.1

Kepert, J. D., & Nolan, D. S. (2014). Reply to Comments on How does the boundary layer contribute to eyewall replacement cycles in axisymmetric tropical cyclones? *Journal of the Atmospheric Sciences*, *71*, 4692–4704. https://doi.org/10.1175/JAS-D-14-0014.1

Kossin, J. P., Schubert, W. H., & Montgomery, M. T. (2000). Unstable interactions between a hurricane's primary eyewall and a secondary ring of enhanced vorticity. *Journal of the Atmospheric Sciences*, *57*, 3893–3917. https://doi.org/10.1175/1520-0469(2001)058<3893:UIBAHS>2.0.CO;2

Kuo, H.-C., Chang, C., Yang, Y., & Jiang, H. (2009). Western North Pacific typhoons with concentric eyewalls. *Monthly Weather Review*, *137*, 3758–3770. https://doi.org/10.1175/2009MWR2850.1

Kuo, H.-C., Cheng, W.-Y., Yang, Y.-T., Hendricks, E. A., & Peng, M. S. (2016). Deep convection in elliptical and polygonal eyewalls of tropical cyclones. *Journal of Geophysical Research: Atmospheres*, *121*, 14456–14468. https://doi.org/10.1002/2016JD025317

Kuo, H. C., Lin, L. Y., Chang, C. P., & Williams, R. T. (2004). The formation of concentric vorticity structures in typhoons. *Journal of the Atmospheric Sciences*, *61*, 2722–2734. https://doi.org/10.1175/JAS3286.1

Kuo, H. C., Schubert, W. H., Tsai, C., & Kuo, Y. (2008). Vortex interactions and barotropic aspects of concentric eyewall formation. *Monthly Weather Review*, *136*, 5183–5198. https://doi.org/10.1175/2008MWR2378.1

Kuo, H. C., Tsujino, S., Huang, C. C., Wang, C. C., & Tsuboki, K. (2019). Diagnosis of the dynamic efficiency of latent heat release and the rapid intensification of Supertyphoon Haiyan (2013). *Monthly Weather Review*, *147*, 1127–1147. https://doi.org/10.1175/MWR-D-18-0149.1

Kuo, H. C., Williams, R. T., & Chen, J. H. (1999). A possible mechanism for the eye rotation of typhoon Herb. *Journal of the Atmospheric Sciences*, *56*, 1659–1673.

Lai, T., Menelaou, K., & Yau, M. K. (2019). Barotropic instability across the moat and inner eyewall dissipation: A numerical study of hurricane Wilma (2005). *Journal of the Atmospheric Sciences*, *76*, 989–1013. https://doi.org/10.1175/JAS-D-18-0191.1

Mallen, K. J., Montgomery, M. T., & Wang, B. (2005). Reexamining the near-core radial structure of the tropical cyclone primary circulation: Implication for the vortex resiliency. *Journal of the Atmospheric Sciences*, *62*, 4088–4425. https://doi.org/10.1175/JAS-3377.1

Martinez, J., Bell, M. M., Rogers, R. F., & Doyle, J. D. (2019). Axisymmetric potential vorticity evolution of Hurricane Patricia (2015). *Journal of the Atmospheric Sciences*, *76*, 2043–2063. https://doi.org/10.1175/JAS-D-18-0373.1

Montgomery, M. T., Abarca, S. F., Smith, R. K., Wu, C., & Huang, Y. (2014). Comments on "How does the boundary layer contribute to eyewall replacement cycles in axisymmetric tropical cyclones?" *Journal of the Atmospheric Sciences*, *71*, 4682–4691. https://doi.org/10.1175/JAS-D-13-0286.1

Montgomery, M. T., & Smith, R. K. (2017). Recent developments in the fluid dynamics of tropical cyclones. *Annual Review of Fluid Mechanics*, *49*, 541–574. https://doi.org/10.1146/annurev-fluid-010816-060022

Powell, M., Vickery, P., & Reinhold, T. (2003). Reduced drag coefficient for high wind speeds in tropical cyclones. *Nature*, *422*, 279–283. https://doi.org/10.1038/nature01481

Powell, M. D. (1982). The transition of the Hurricane Frederic boundary-layer wind field from the open Gulf of Mexico to landfall. *Monthly Weather Review*, *110*, 1912–1932. https://doi.org/10.1175/1520-0493(1982)110<1912:TTOTHF>2.0.CO;2

Rozoff, C. M., Schubert, W. H., & Kossin, J. P. (2008). Some dynamical aspects of tropical cyclone concentric eyewalls. *Quarterly Journal of the Royal Meteorological Society*, *134*, 583–593. https://doi.org/10.1002/qj.237

Samsury, C. E., & Zipser, E. J. (1995). Secondary wind maxima in hurricanes: Airflow and relationship to rainbands. *Monthly Weather Review*, *123*, 3502–3517. https://doi.org/10.1175/1520-0493(1995)123<3502:SWMIHA>2.0.CO;2

Sanabia, E. R., Barrett, B. S., Celone, N. P., & Cornelius, Z. D. (2015). Satellite and aircraft observations of the eyewall replacement cycle in Typhoon Sinlaku (2008). *Monthly Weather Review*, *143*, 3406–3420. https://doi.org/10.1175/MWR-D-15-0066.1

Schubert, W. H. (2018). *Bernhard haurwitz memorial lecture (2017): Potential vorticity aspects of tropical dynamics* (p. 27). arXiv:1801.08238 [physics.ao-ph]. Retrieved from https://arxiv.org/abs/1801.08238

Shapiro, L. J. (1983). The asymmetric boundary layer flow under a translating hurricane. *Journal of the Atmospheric Sciences*, *40*, 1984–1998. https://doi.org/10.1175/1520-0469(1983)040<1984:TABLFU>2.0.CO;2

Sitkowski, M., Kossin, J. P., & Rozoff, C. M. (2011). Intensity and structure changes during hurricane eyewall replacement cycles. *Monthly Weather Review*, *139*, 3829–3847. https://doi.org/10.1175/MWR-D-11-00034.1

Slocum, C. J. (2018). *The role of inner-core and boundary layer dynamics on tropical cyclone structure and intensification* (p. 106). Dissertation, Colorado State University.

Smith, R. K., & Montgomery, M. T. (2016). The efficiency of diabatic heating and tropical cyclone intensification. *Quarterly Journal of the Royal Meteorological Society*, *142*, 2081–2086. https://doi.org/10.1002/qj.2804

Smith, R. K., & Montgomery, M. T. (2020). The generalized Ekman model for the tropical cyclone boundary layer revisited: The myth of inertial stability as a restoring force. *Quarterly Journal of the Royal Meteorological Society*, *146*, 3435–3449.

Smith, R. K., Montgomery, M. T., & Van Sang, N. (2009). Tropical cyclone spin-up revisited. *Quarterly Journal of the Royal Meteorological Society*, *135*, 1321–1335. https://doi.org/10.1002/qj.428

Tsujino, S., Horinouchi, T., Tsukada, T., Kuo, H.-C., Yamada, H., & Tsuboki, K. (2021). Inner-core wind field in a concentric eyewall replacement of typhoon Trami (2018): A quantitative analysis based on the Himawari-8 satellite. *Journal of Geophysical Research: Atmospheres*, *126*, e2020JD034434. https://doi.org/10.1029/2020JD034434

Tsujino, S., & Kuo, H.-C. (2020). Potential vorticity mixing and rapid intensification in the numerically simulated Supertyphoon Haiyan (2013). *Journal of the Atmospheric Sciences*, *77*, 2067–2090. https://doi.org/10.1175/JAS-D-19-0219.1

Tsujino, S., Tsuboki, K., & Kuo, H. C. (2017). Structure and maintenance mechanism of long-lived concentric eyewalls associated with simulated Typhoon Bolaven (2012). *Journal of the Atmospheric Sciences*, *74*, 3609–3634. https://doi.org/10.1175/JAS-D-16-0236.1

Williams, G. J. (2015). The effects of vortex structure and vortex translation on the tropical cyclone boundary layer wind field. *Journal of Advances in Modeling Earth Systems*, *7*, 188–214. https://doi.org/10.1002/2013MS000299

Williams, G. J. (2017). The thermodynamic evolution of the hurricane boundary layer during eyewall replacement cycles. *Meteorology and Atmospheric Physics*, *129*, 11–627. https://doi.org/10.1007/s00703-016-0495-4

Williams, G. J., Taft, R. K., McNoldy, B. D., & Schubert, W. H. (2013). Shock-like structures in the tropical cyclone boundary layer. *Journal of Advances in Modeling Earth Systems*, *5*, 338–353. https://doi.org/10.1002/jame.20028

Willoughby, H. E., & Black, P. G. (1996). Hurricane Andrew in Florida: Dynamics of a disaster. *Bulletin of the American Meteorological Society*, *77*, 543–550. https://doi.org/10.1175/1520-0477(1996)077<0543:HAIFDO>2.0.CO;2

Willoughby, H. E., Clos, J. A., & Shoreibah, M. G. (1982). Concentric eye walls, secondary wind maxima, and the evolution of the hurricane vortex. *Journal of the Atmospheric Sciences*, *39*, 395–411. https://doi.org/10.1175/1520-0469(1982)039<0395:CEWSWM>2.0.CO;2

Wood, V. T., White, L. W., Willoughby, H. E., & Jorgensen, D. P. (2013). A new parametric tropical cyclone tangential wind profile model. *Monthly Weather Review*, *141*, 1884–1909. https://doi.org/10.1175/MWR-D-12-00115.1

Yang, Y.-T., Hendricks, E. A., Kuo, H.-C., & Peng, M. S. (2014). Long-lived concentric eyewalls in typhoon Soulik (2013). *Monthly Weather Review*, *142*, 3365–3371. https://doi.org/10.1175/MWR-D-14-00085.1

Yang, Y.-T., Kuo, H.-C., Hendricks, E. A., Liu, Y.-C., & Peng, M. S. (2015). Relationship between typhoons with concentric eyewalls and ENSO in the western North Pacific basin. *Journal of Climate*, *28*, 3612–3623. https://doi.org/10.1175/JCLI-D-14-00541.1

Yang, Y.-T., Kuo, H.-C., Hendricks, E. A., & Peng, M. S. (2013). Structural and intensity changes of concentric eyewall typhoons in the western North Pacific basin. *Monthly Weather Review*, *141*(8), 2632–2648. https://doi.org/10.1175/MWR-D-12-00251.1

Yang, Y.-T., Kuo, H.-C., Tsujino, S., Chen, B.-F., & Peng, M. S. (2021). Characteristics of the long-lived concentric eyewalls in tropical cyclones. *Journal of Geophysical Research: Atmospheres*, *126*, e2020JD033703. https://doi.org/10.1029/2020JD033703

Zhang, J. A., & Montgomery, M. T. (2012). Observational estimates of the horizontal eddy diffusivity and mixing length in the low-level region of intense hurricanes. *Journal of the Atmospheric Sciences*, *69*, 1306–1316. https://doi.org/10.1175/JAS-D-11-0180.1

Zhou, X., & Wang, B. (2011). Mechanism of concentric eyewall replacement cycles and associated intensity changes. *Journal of the Atmospheric Sciences*, *68*, 972–988. https://doi.org/10.1175/2011JAS3575.1